Article

Not peer-reviewed version

A Multispectral Camera Suite for the Observation of Earth's Outgoing Radiative Energy

Steven Dewitte [*] , Al Ameen Abdul Nazar , Yuan Zhang , Lien Smeesters

Posted Date: 20 October 2023

doi: 10.20944/preprints202310.1346.v1

Keywords: earth energy imbalance; reflected solar radiation; outgoing longwave radiation; optical design

doi:10.20944/preprints202310.1346.v1

Article

A Multispectral Camera Suite for the Observation of Earth's Outgoing Radiative Energy

Steven Dewitte [1,*,†], Al Ameen Abdul Nazar [1,2,†], Yuan Zhang [1,3] and Lien Smeesters[2]

[1] Royal Observatory of Belgium, Avenue Circulaire 3, 1180 Brussels, Belgium
[2] Brussels Photonics (B-PHOT), Applied Physics and Photonics Department, Vrije Universiteit Brussel, Pleinlaan 2, 1050 Brussels, Belgium;
[3] Key Laboratory of Thermo-Fluid Science and Engineering, Ministry of Education, School of Energy and Power Engineering, Xi'an Jiaotong University, Xi'an 710049, China
* Correspondence: steven.dewitte@oma.be
† These authors contributed equally to this work.

Abstract: As part of the Earth Climate Observatory space mission concept for the direct observation from space of the Earth Energy Imbalance, we propose an advanced camera suite for the high resolution observation of the Total Outgoing Radiation of the Earth. For the observation of the Reflected Solar Radiation, we propose the use of two multispectral cameras covering the range from 400 to 950 nm, with a nadir resolution of 1.7 km, combined with a high resolution RGB camera, with a nadir resolution of 0.57 km. For the observation of the Outgoing Longwave Radiation, we propose the use of 6 microbolometer cameras, with each a spectral bandwidth of 1 μm in the range from 8 to 14 μm, and with a nadir resolution of 2.2 km.

Keywords: Earth Energy imbalance; Reflected Solar Radiation; Outgoing Longwave Radiation; optical design

0. Introduction

The Earth Energy Imbalance (EEI) is defined as the small difference between the incoming energy received by the Earth from the Sun, and the outgoing energy lost by the Earth to space. Both the incoming solar and the terrestrial outgoing energy are of the order of 340 W/m^2 at the global annual mean level [1], while the EEI is of the order of 0.9 W/m^2 [2,3]. The EEI is accumulated in the Earth climate system, particularly in the oceans which have a high heat capacity, and results in global temperature rise.

The monitoring of the EEI is of prime importance for a predictive understanding of climate change [4,5]. In particular, monitoring of the EEI gives an early indication on how well mankind is doing in implementing the Paris Climate Agreement.

Despite its fundamental importance, the EEI is currently poorly measured from space, due to two fundamental challenges.

The first fundamental challenge is that the EEI is the difference between two opposite terms with nearly equal amplitude. Currently the incoming solar radiation and outgoing terrestrial radiation are measured with separate instruments, which means that their calibration errors are added, and overwhelm the signal to be measured. The current error on the direct measurement of the EEI is of the order of 5 W/m^2 [1], significantly larger than the signal to be measured of the order of 0.9 W/m^2. In order to make significant progress in this challenge, a differential measurement using identically designed, intercalibrated instruments - so-called Wide Field Of View (WFOV) radiometers - to measure both the incoming solar radiation and the outgoing terrestrial radiation, is needed [6].

The second fundamental challenge, is that the outgoing terrestrial radiation has a systematic diurnal and annual cycle. From 2003 to 2023, the diurnal cycle of the outgoing terrestrial radiation was sampled from the so-called morning and afternoon Sun synchronous orbits, complemented by geostationary imagers [7,8]; recently the sampling from the morning orbit had to be abandonned [9].

The sampling of the diurnal cycle can be improved, by using two orthogonal 90° inclined orbits [10] which provide both global coverage, and a statistical sampling of the full diurnal cycle at the seasonal (3 month) time scale.

The wide field of view radiometer will make accurate low resolution measurements of the Total Outgoing Radiation (TOR) of the Earth. Auxiliary visible and thermal imagers will be used to increase the spatial resolution of the radiometer observations, and to separate the TOR spectrally in the Reflected Solar Radiation (RSR) and the Outgoing Longwave Radiation (OLR). Figure 1 shows a multi-annual mean TOR at 1° resolution, Figure 2 shows the corresponding RSR, and Figure 3 shows the corresponding OLR.

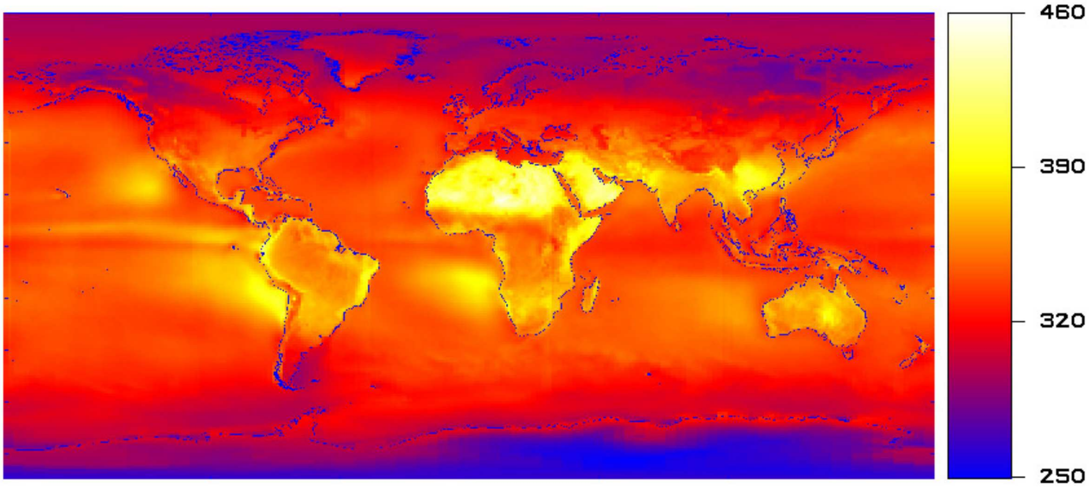

Figure 1. Multi-annual mean Total Outgoing Radiation at 1° resolution. Unit: W/m^2. Reproduced from [1].

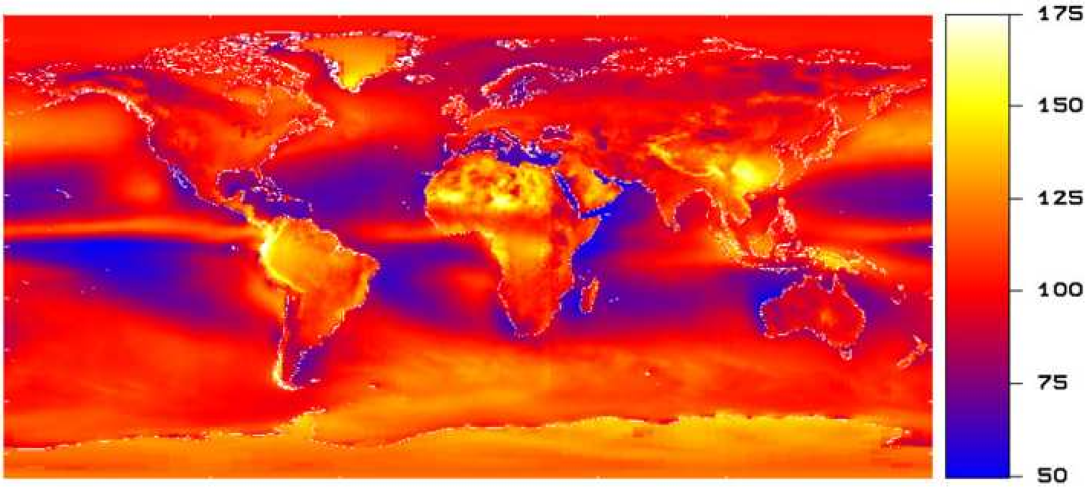

Figure 2. Multi-annual mean Reflected Solar Radiation at 1° resolution. Unit: W/m^2. Reproduced from [1].

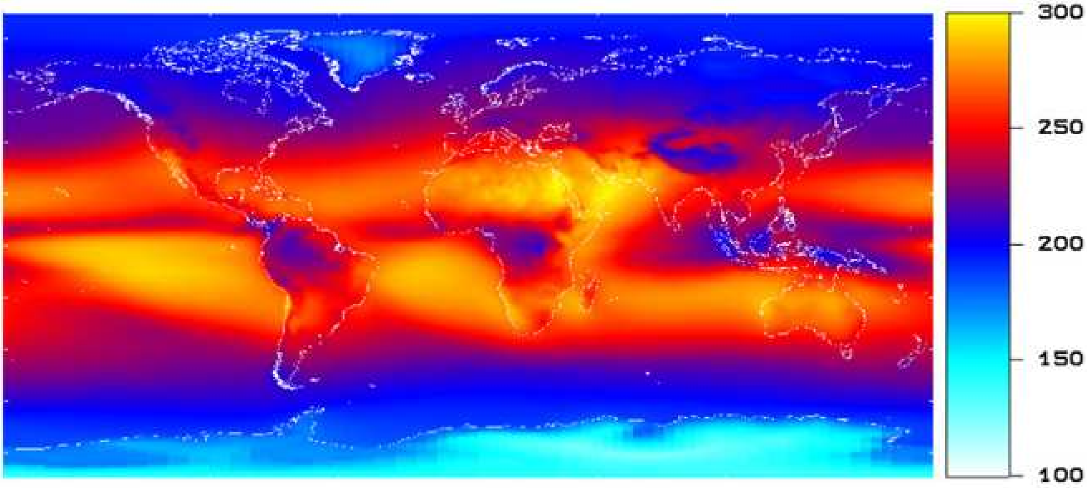

Figure 3. Multi-annual mean Outgoing Longwave Radiation at 1° resolution. Unit: W/m^2. Reproduced from [1].

A reference design of the visible imager is described in [11].

A reference design of the thermal imager is described in [12].

A new space mission concept, called the Earth Climate Observatory (ECO) for the accurate and stable monitoring of the EEI, is currently elaborated , building further on the basic concepts of [6,11,12].

In this paper we describe an advanced multispectral camera suite with performance that goes beyond the [11,12] reference designs in terms of spectral information content. In section 1, we describe the advanced shortwave camera suite. In section 2, we describe the optical design for a new visible high resolution camera used in the advanced shortwave camera suite. In section 3 we develop the advanced longwave camera suite. We discuss our results in section 4, and provide our conclusions in section 5.

1. Shortwave camera suite

In the [11] reference design, the ShortWave (SW) camera - also called solar camera - consists of an RGB CMOS detector array with a wide field of view lens allowing to view the Earth from limb to limb. The field of view is 140 °. The Wide Field Of View (WFOV) lens design is illustrated in Figure 4. The nadir resolution is 2.2 km. The f-number is 3. The used RGB CMOS spectral responses are illustrated in Figure 5. On a stand alone basis the RSR can be estimated from an RGB CMOS imager through spectral regression with a noise level of 3 %.

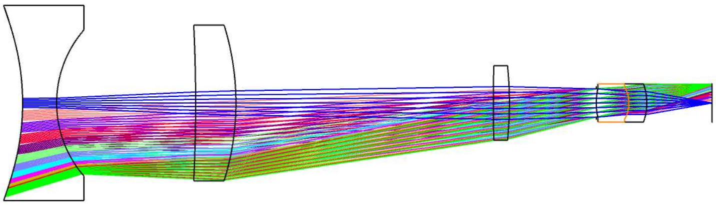

Figure 4. Wide field of view reference lens design for the SW camera. Reproduced from [11].

The only on-board calibration source for the SW camera suite will be a shutter, allowing to verify the dark current, and also allowing to shield the camera from direct solar illumination during solar pointing. The camera spectral gains and dark current will be determined pre-flight during ground calibration. The stability of the RGB spectral responses and the gains will be monitored, and if needed adjusted in-flight through vicarious calibration monitoring stable Earth targets similar to [13–15].

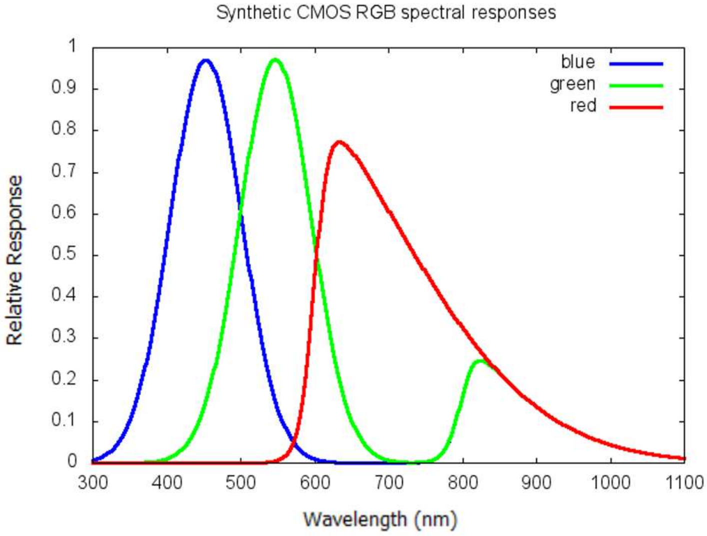

Figure 5. RGB CMOS spectral responses used in [11].

The spectral regression noise level by which the RSR broadbance radiance can be estimated, can be improved by increasing the number of narrowband spectral channels used as input for the regression. In [16] a commercially available CMOS sensor with 4x4 filter bands in the VIS (470-620nm) is described. Also a commercially available CMOS sensor with 5x5 filter bands in the VIS-NIR (650-975nm) is described.

The newly proposed ECO Shortwave Camera Suite (SCS) consists of 3 separate ShortWave (SW) cameras. Camera 2 and 3 can be based on the same CMOSIS CMV2000 sensor array. Since the size of the detector is comparable to the detector used in [11], the reference wide field of view lens from Figure 4 can be re-used. Camera 1 can be realized using the higher resolution CMOSIS CMV12000 sensor array. Since the size of the CMV12000 sensor is about 3 times larger than the detector size used in [11], a new lense design is appropriate, and will be presented in section 2.The 3 shortwave cameras, have different spectral responses, by using different filters directly integrated on the CMOS chip, with spatial patterns illustrated in Figure 6.

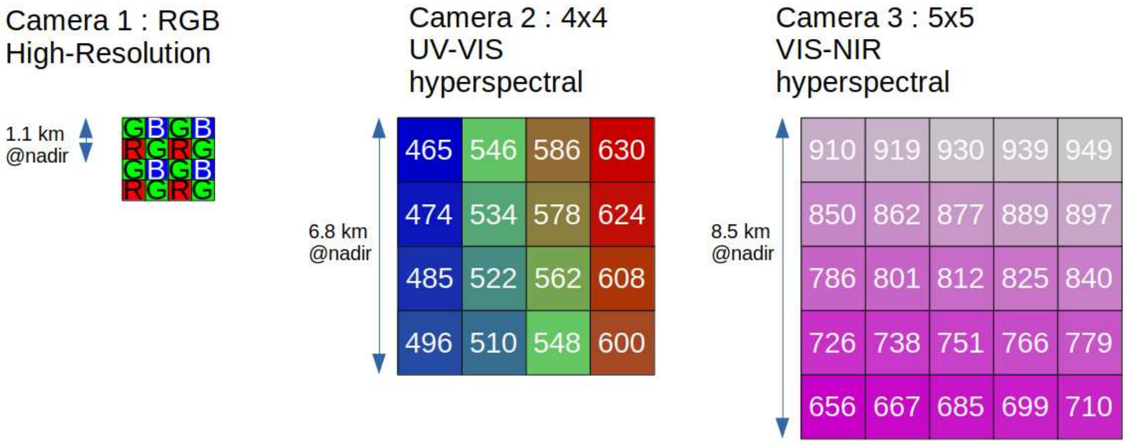

G	B	G	B
R	G	R	G
G	B	G	B
R	G	R	G

465	546	586	630
474	534	578	624
485	522	562	608
496	510	548	600

910	919	930	939	949
850	862	877	889	897
786	801	812	825	840
726	738	751	766	779
656	667	685	699	710

Figure 6. Realization of the ECO SW camera suite, using 3 separate cameras.

The 3 ECO SW cameras are the following:

1. ECO SW Camera 1 will be the RGB high-resolution SW camera, formed by a CMOS sensor, with spectral response between 400 and 1000 nm, with standard 'RGGB' Bayer pattern. The active

area of the CMOS sensor will be 3000*3000 pixels, yielding a nadir resolution for a single pixel of 0.57 km, and a nadir resolution for the 2x2 RGGB pixels of 1.1 km. The pixel pattern of SW camera 1 is illustrated in the left part of Figure 6.

2. ECO SW Camera 2 will be the VIS SW camera from [16]. The nadir resolution of the 4x4 VIS filter pattern - illustrated in the middle part of Figure 6 - is 6.8 km.
3. ECO SW Camera 3 will be the VIS-NIR SW camera from [16], using the same underlying CMOS sensor as Camera 2. The nadir resolution of the 5x5 VIS-NIR filter pattern - illustrated in the right part of Figure 6 - is 8.5 km.

The detectors from [16], considered for camera 2 and 3, are also considered for the CubeMAP [17] and Hyperscout-H [18] space missions.

2. Optical design high-resolution SW camera

The SW camera uses the CMOSIS CMV12000 4K CMOS detector with pixel size 5.5 μm. For the envisioned FOV of 140°, we use a circular area of 16.5 mm diameter, corresponding to 3000 pixels. For a WFOV lens with field angle 140° observing the Earth from an altitude of 700 km, the size of the nadir pixel is 0.57 km. Considering that the sensor is used with a Bayer color filter, the RMS spot size we require should be smaller than 2 pixels - corresponding to 11 μm. The barrel distortion is considered to be corrected in post processing.

2.1. The Design parameters

The lens train - illustrated in Figure 7 - consist of 6 lenses, two of which form an achromatic doublet. The doublet along with the third lens works as a chromatic aberration correction system along with focusing the image on the image plane. The main lens properties are summarised in Table 1. The Lens materials were selected from the SCHOTT ® catalog. The LAK14 is a crown glass with relatively high refractive index and SF6 is a flint glass with high refractive index as well.

There are 3 aspherical surfaces on the system. the first surface, the last surface and the final surface of the achromatic doublet. This is done to ensure increased light collection and to reduce spherical aberrations. The initial reference design for this lens train was the one shown in Figure 4 [11].

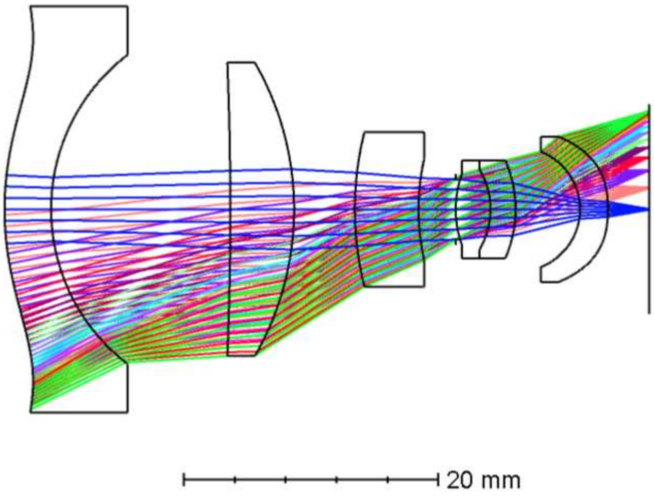

Figure 7. Optical design of the SW camera. The total axial length equals 50.6 mm. The lens train consists of 4 singlet (s) lenses and an acromatic doublet (d) arranged in a s-s-s-d-s format. The detector has a size of 16.5 × 16.5 mm. The FOV is 140°. The 12 different colors pertain to 12 different angles between 0° and 70° with a step of 6.36°.

Table 1. Lens data: Surface type, Material, thickness and diameters. Three aspherical surfaces. s-s-s-d-s format.

Lens order (singlet/doublet)	Front surface type	Rear surface type	Material	Thickness (mm)	Diameter (mm)
First lens (s: singlet)	Aspherical	Spherical	LAK14	3.7	32
Second lens (s)	Spherical	Spherical	LAK14	5	23
Third lens (s)	Spherical	Spherical	SF6	5	12
Fourth lens (d: doublet)	Spherical	Spherical	N-FK51A	2.7	7.6
Fifth lens (d)	Spherical	Aspherical	N-SF6	2	7.6
Sixth lens (s)	Spherical	Aspherical	LAK14	2.2	11.4

The system was designed and optimised using the Zemax OpticStudio® software. Only a few parameters were constrained, namely, the 'Effective focal length', at 15.6 mm, the lens thickness minimum being 2 mm. The initial merit function for spot size was done through the 'Quick focus' function provided by Zemax. Once a substantial percentage of criteria is fulfilled during optimization and satisfactory RMS values along with a good relative illumination were achieved, further optimization was done using the 'Hammer optimization' function provided by Zemax.

2.2. Optical performance

2.2.1. RMS error

The RMS error - see Figure 8 - shows the root mean square deviation of a bunch of rays of light from its intended spot of incidence. This value is supposed to be below 11μm approximately. This is widely true for the said lens train and only reaches 12μm for the 400 nm wavelength at the extreme 70° incidence angle. This can be considered sufficient for our purposes.

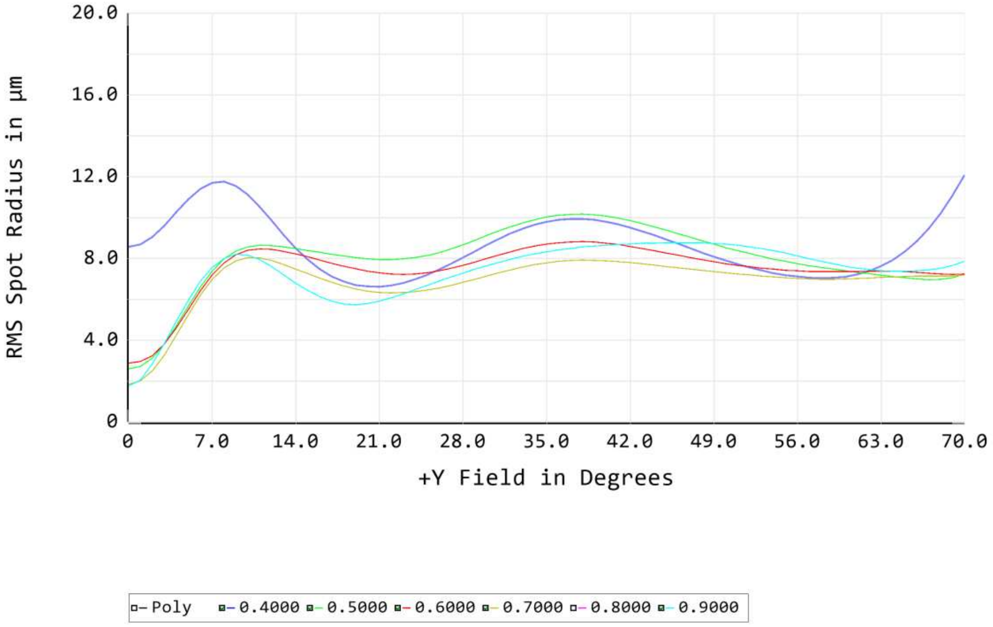

Figure 8. The RMS error shown in μm versus incidence angle of the light on the first surface of the lens. the colors depict various wavelengths of light (in μm).

2.2.2. Seidel aberrations

The Seidel aberrations - see Figure 9 - apart from distortion have been optimized and kept low. The distortion/ barrel distortion is to be corrected on ground as post-processing.

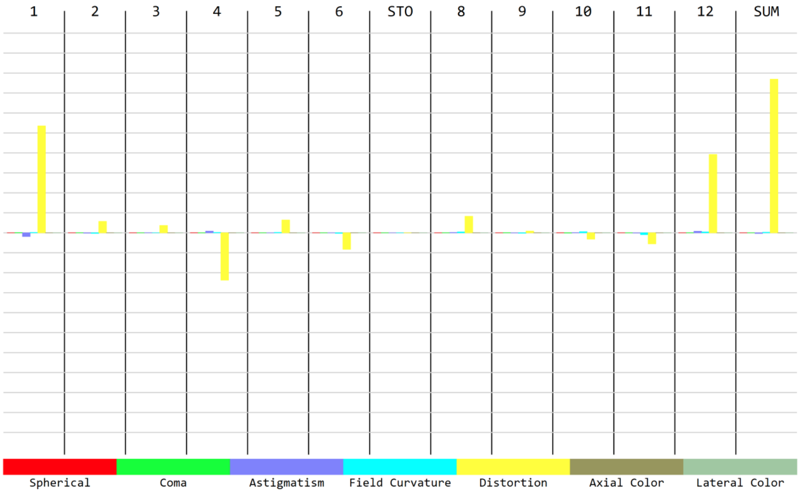

Figure 9. The five different Seidel aberrations and chromatic aberrations.The largest contributor being the barrel distortion.

2.2.3. Point Spread Function (PSF)

The optical PSF is the characterization of how a point of light is transformed when passing through an optical system. The optical PSF is related to the RMS spot size as shown in Figure 8, which mostly lies below the desired 11 μm. The average optical PSF of all wavelengths is given in Figure 10.

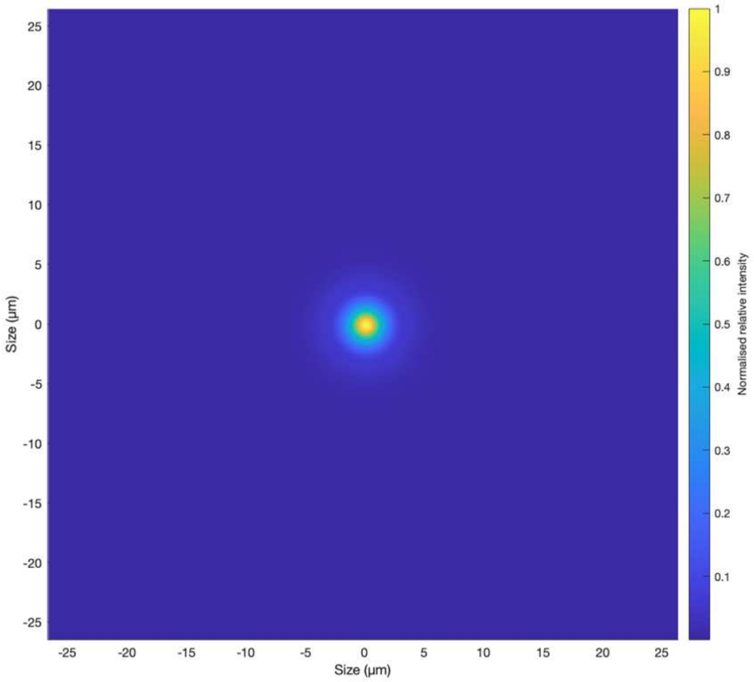

Figure 10. The average optical PSF of all simulated wavelengths for the 0° incidence angle. Image size 53.236 by 53.236 μm.

To evaluate the joint effect of the optical PSF, and the pixel shape, we calculate the convolution op the optical PSF with the detector pixel shape. We use a layer of fixed size containing several pixels of the same type, either Red/Blue active pixels or Green-Green active pixels. The two types of pixels exist due to the presence of the Bayer filter. The individual pixels have sizes of 5.5μm but to emulate real pixels, we use an active area of 80% of the nominal pixel size as shown in Figure 11. We assume the variation of the optical PSF is negligeable within the layer of pixels.

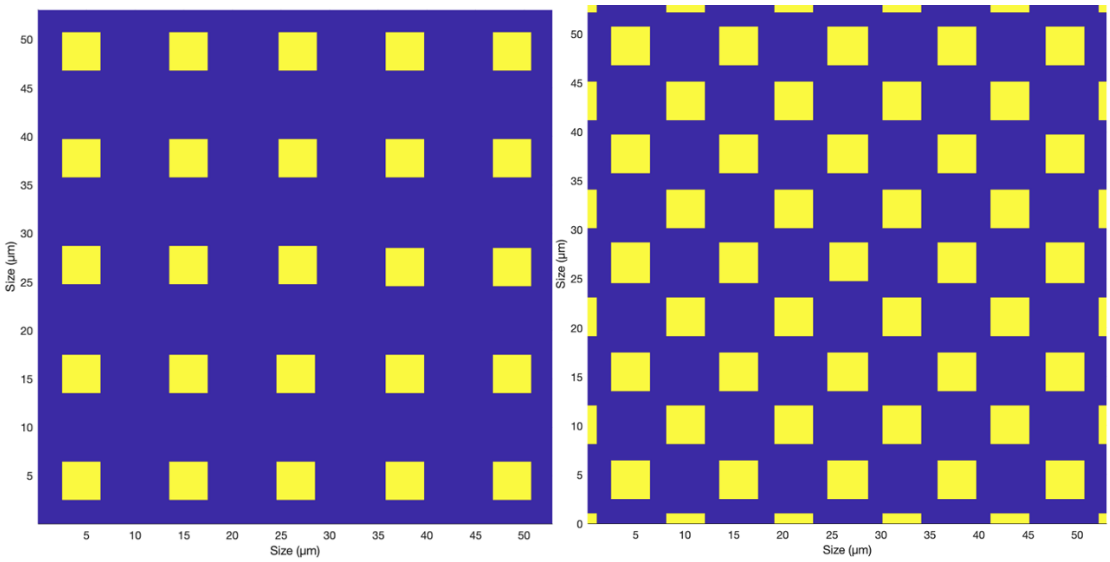

Figure 11. The active pixel layer of type (a)Red/Blue pixels, (b) Green-Green pixels, for a fixed detector area of 53.236 by 53.236 μm, where individual pixels cover 80% of a nominal 5.5μm square area.

The convolution of these pixel layers with the optical PSF for the 0° incidence angle, is shown in Figure 12. It can be seen that, after the convolution, individual pixels are still recognisable.

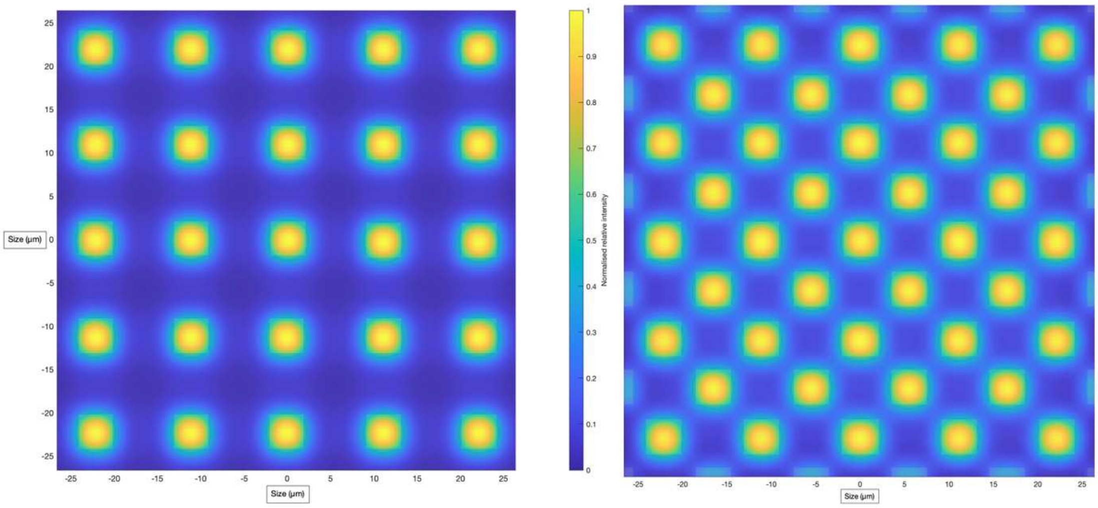

Figure 12. The convolution of active pixel layer of type (a)Red/Blue, (b) Green-Green with the PSF of 0° incident light, where individual pixels are overlaid over the convolution.

From the RMS Figure 8, we see that the 400 nm wavelength at 70° incidence angle and 500 nm at 38° incidence angles have high RMS spot radius. We therefore examine in detail the PSFs and convolutions at these particular wavelengths and angles.

The optical PSF for light with a wavelength of 400 nm incident at 70°, is shown in the left of Figure 10. The convolution of this optical PSF with the blue-type active pixel layer is shown in the right of Figure 10.

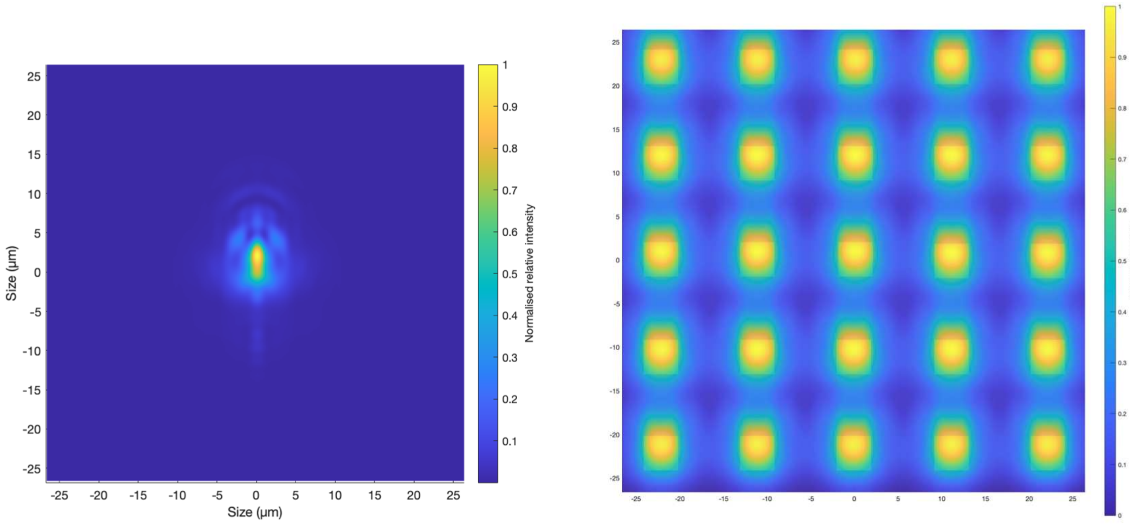

Figure 13. Left: The PSF of 400 nm wavelength for 70° incidence angle. Image size 53.236 by 53.236 μm. Right: The convolution of active pixel layer of blue-type with the PSF of 70° incident light of 400 nm wavelength, where individual pixels are overlaid over the convolution.

The optical PSF for light with a wavelength of 500 nm incident at 38°, is shown in the left of Figure 14. The convolution of this optical PSF with the green-type active pixel layer is given in the right of Figure 10.

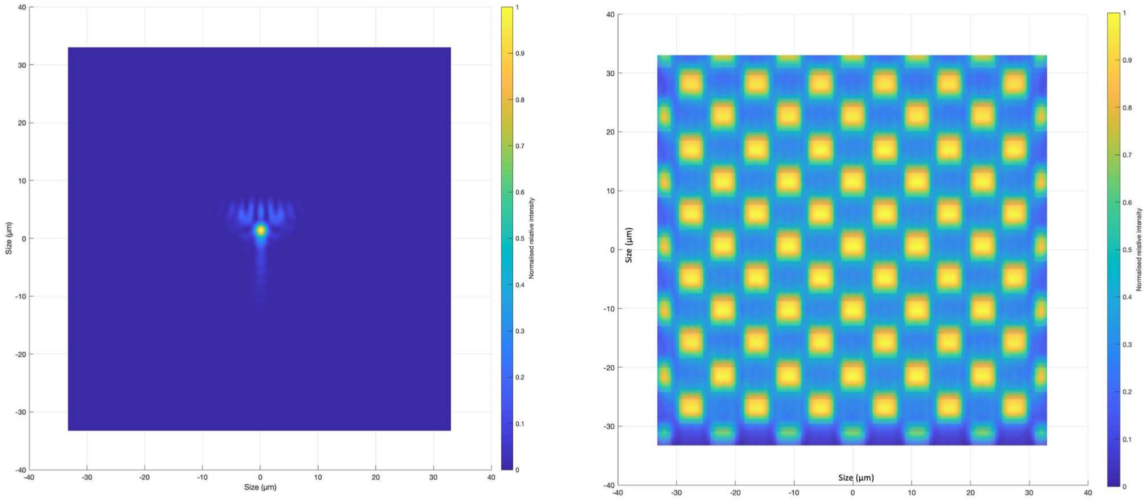

Figure 14. Left: The PSF of 500 nm wavelength for 38° incidence angle. Image size 66.545 by 66.545 μm. Right: The convolution of active pixel layer of green-type with the PSF of 38° incident light of 500 nm wavelength, where individual pixels are overlaid over the convolution.

We see that the light spreads towards the top and bottom of the pixels in the right part of Figures 13 and 14. However, these spreads are acceptable for the function of the detector.

2.2.4. Relative intensity

The relative intensity of light as a function of angle of incidence is shown in Figure 15.

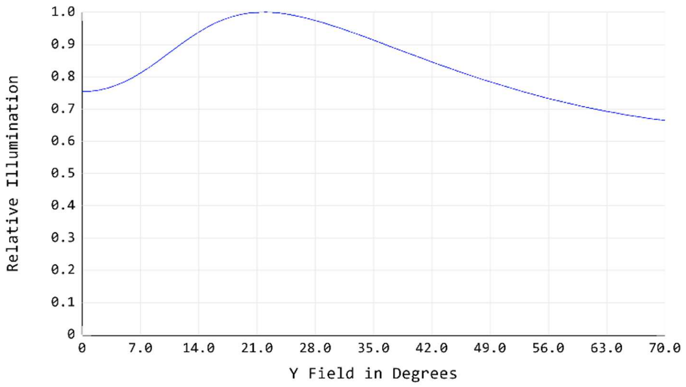

Figure 15. The relative intensity versus the angle of incidence.

2.2.5. Chromatic aberration

The chromatic aberration of the system is that of a compensated system as shown in Figure 16.

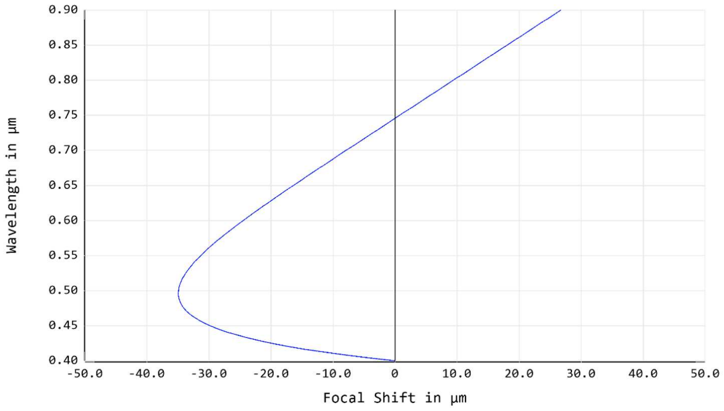

Figure 16. Chromatic aberration of the entire optical system.

2.3. *Simulated Performance for Earth observation*

2.3.1. SNR High-resolution 4K-RGB camera

For camera 1, with a nadir resolution of 570 m, and a nominal satellite altitude of 700 km, Lambertian Earth leaving flux is attenuated towards the entrance of the camera by a factor $(0.57/700)^2/\pi = 2.11 \times 10^{-7}$. Within the optical system, with a 0° radiometric aperture diameter of 5.38 mm, and a detector pixel size of 5.5 micron, the entrance flux is amplified towards the detector by a factor $\pi/4 \times (5.38/5.5 \times 10^{-3})^2 = 7.5 \times 10^5$. Assuming no light loss, the ratio between the detector flux and the Earth flux is then $2.11 \times 10^{-7} \times 36.7 \times 10^4 = 0.16$. Assuming a 50 % light loss, the ratio becomes $0.16 \times 0.5 = 0.08$.

The detector for camera 1, is the CMOSIS CMV12000 CMOS detector array, with 4096×3072 pixels, and a full well capacity of 1485 counts, corresponding to approximately 10.5 bit per pixel. For a 3000×3000 pixel subarray, it can be read out at a maximum frame rate of 400 fps, corresponding to a minimum readout time for a single frame of 2.5 ms. We calculate the maximum integration time before saturation occurs for the theoretical case of 100 % diffuse reflection for an incident solar irradiance of 1500 $\mathrm{W/m^2}$. The wavelength dependent saturation time for Red, Green and Blue wavelengths with peaks at 634 nm, 547 nm, 453 nm respectively, are 16.7 μs, 18.9 μs , 26 μs respectively. An average Quantum efficiency of 0.45 is assumed.

Before motion blurring occurs, a further time averaging is allowed within a time period of 0.57 km / (7 km/s)= 81.4 ms, so over $81.4ms/2.5ms \approx 32$ frames. The SNR as a function of wavelength for 32 integrations of 15 μs each for red, green and blue wavelengths are 47×10^3, 41×10^3 and 30×10^3 respectively. If we follow the procedure of [11] to estimate the RSR from the RGB camera measurements, the quantisation errors corresponding to these SNR values cause an error on the RSR of 0.04 W/m^2. This 0.04 W/m^2 quantisation error, is small compared to the [11] spectral regression error of 3 %, which for the reference scene of 1500 W/m^2 corresponds to 3 % × 1500 W/m^2 = 45 W/m^2.

2.3.2. SNR multispectral cameras

For cameras 2 and 3, with a nadir resolution of 1.71 km, and a nominal satellite altitude of 700 km, Lambertian Earth leaving flux is attenuated towards the entrance of the camera by a factor $(1.71/700)^2/\pi = 1.9 \times 10^{-6}$. Within the optical system, with a 0° radiometric aperture diameter of 1.14 mm, and a detector pixel size of 5.5 micron, the entrance flux is amplified towards the detector by a factor $\pi/4 \times (1.14/5.5 \times 10^{-3})^2 = 3.37 \times 10^4$. The ratio between the detector flux and the Earth flux is then $1.9 \times 10^{-6} \times 3.37 \times 10^4 = 0.064$ without light loss, and $0.064 \times 0.5 = 0.032$ with 50 % light loss.

The detector for camera 2 and 3 is the CMOSIS CMV2000 CMOS detector array, with 1024×2048 pixels, and a full well capacity of 1012.5 counts, corresponding to ≈ 10 bit per pixel. For a 1000×1000 pixel subarray, it can be read out at a maximum frame rate of 680 fps, corresponding to a minimum readout time for a single frame of 1.47 ms. Before motion blurring occurs, a further time averaging is allowed within a time period of 1.71 km / 7 km/s = 243 ms, so over $243ms/1.47ms \approx 166$ frames. The Signal to Noise Ratio (SNR) as a function of wavelength for 166 readouts of 400 μs each is illustrated in Figure 17. For the least sensitive wavelength at 950 nm, the SNR for a single readout is 771, the SNR for 166 readouts is 128×10^3.

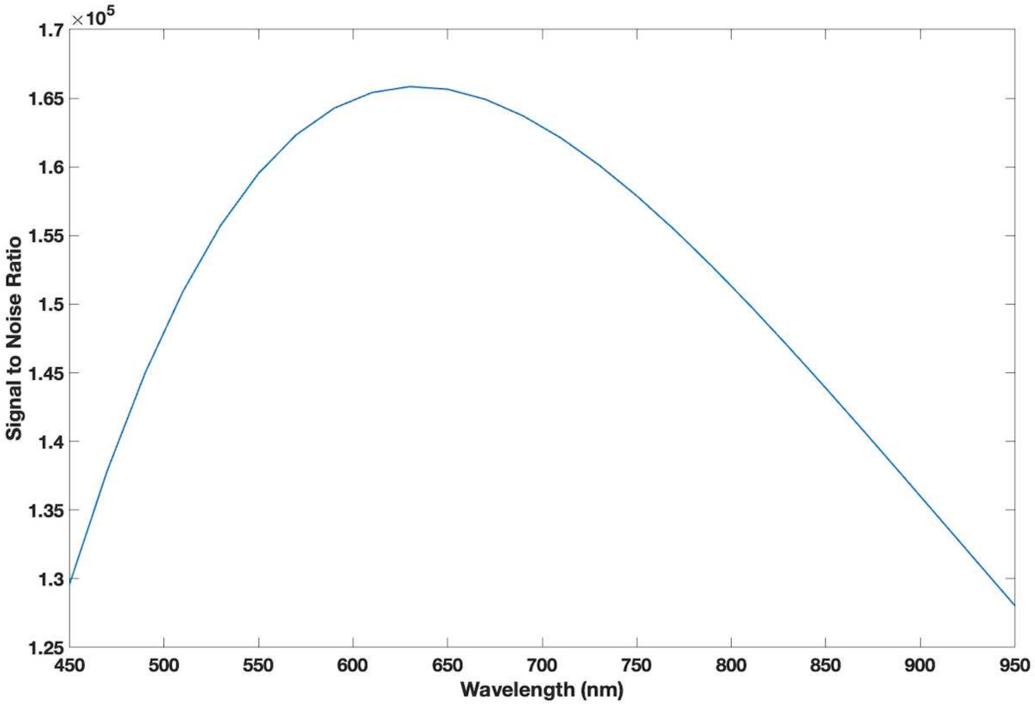

Figure 17. 166 integration signal to Noise ratio versus wavelength of multispectral cameras.

3. Longwave camera suite

3.1. Multispectral thermal cameras

A reference design of the thermal imager is described in [12]. The thermal imager consists of a microbolometer detector array with a WFOV lens allowing to view the Earth from limb to limb. The WFOV lens design is illustrated in Figure 18. The nadir sampling distance is 2.2 km, and the nadir

doi:10.20944/preprints202310.1346.v1

effective resolution is 4.4 km. Using a single wavelength band of 8-14 micron, on a stand alone basis the OLR can be estimated from the thermal imager with an accuracy of 5 %.

The LongWave (LW) cameras will be equipped with a shutter with known temperature and known high emissivity. This shutter will act as a flat blackbody. Combined with the deep space view a two-point in-flight calibration for the longwave cameras will be implemented. The shutter view will be used for the characterization of the thermal offset as a function of the lens temperature. The deep space view will be used for an in-flight verification of the gain, that will also be measured on the ground before flight.

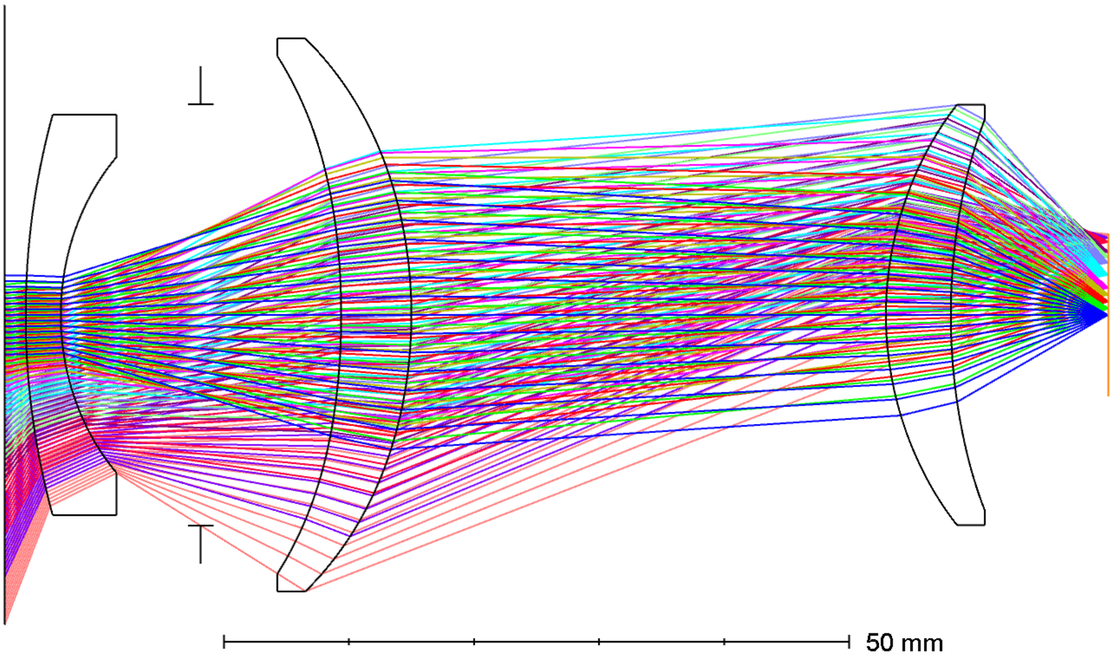

Figure 18. Wide field of view reference lens design for the thermal camera.

For improving the spectral regression OLR noise level, the number of ECO LW channels can be increased. This will be done by using multiple cameras, with filters inserted in front of the microbolometer detector array. In [19], the TIRI/HERA space instrument is described using the same detector as in [12], and a filter wheel with 6 filters each having a bandwidth of approximately 1 μm. For ECO we will adopt similar filters, listed in Table 2.

Table 2. ECO longwave spectral bands. The limits are defined at the FWHM (Full Width at Half Maximum) of the spectral bands.

Band	Limits
LW-1	8-9 μm
LW-2	9-10 μm
LW-3	10-11 μm
LW-4	11-12 μm
LW-5	12-13 μm
LW-6	13-14 μm

The 6 ECO filter spectral responses are also similar to filter responses used for the SEVIRI/MSG [20] and FCI/MTG [21] instruments.

The ECO LW Camera Suite (LCS) will be formed by 6 separate LW cameras, each consisting of the same microbolometer array and WFOV lens, and each equiped with a different filter realising the

doi:10.20944/preprints202310.1346.v1

spectral responses from Table 2. For the microbolometer array, the Lynred 1024x768 array with 17 μm pixel pitch [22] can be used.

The LW spectral responses are illustrated in Figure 19.

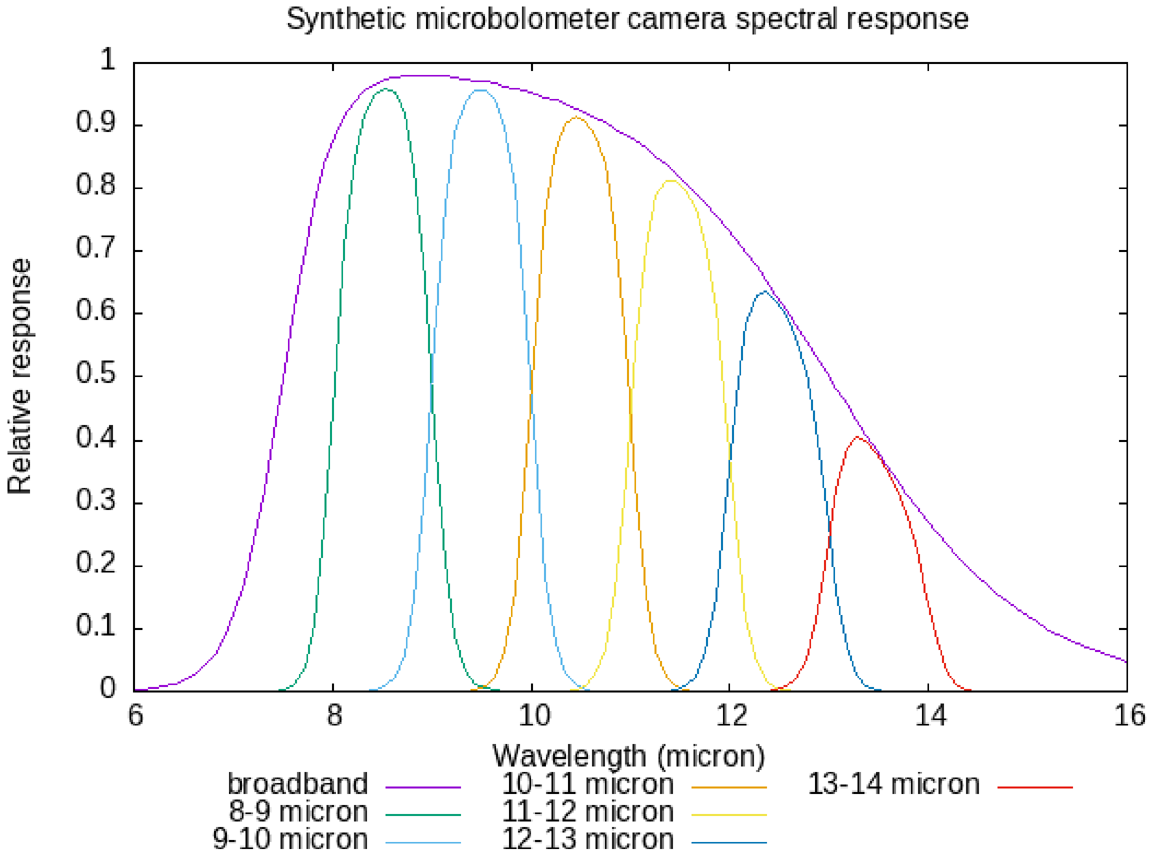

Figure 19. Longwave spectral responses.

3.2. Noise Equivalent Differential Temperature (NEDT)

For the thermal cameras, with a nadir sampling distance of 2 km, and a nominal satellite altitude of 700 km, Lambertian Earth leaving flux is attenuated towards the entrance of the camera by a factor $(2/700)^2$=8.2×10^{-6}. Within the optical system, with a 0° radiometric aperture diameter of 6.61 mm, and a detector pixel size of 17 micron, the entrance flux is amplified towards the detector by a factor $\pi/4$*$(6.61/17\times10^{-3})^2$ = 119×10^3. Asssuming no light loss, the ratio between the detector flux and the Earth flux is then 8.2×10^{-6} * 119×10^3 = 0.97. Assuming 50 % light loss, the ratio becomes 0.97 * 0.5 = 0.49.

The Lynred 1024x768 microbolometer detector array has an NEDT of 50 mK for a f/1 optics at 300 K and at 30 Hz. For the above calculated optical magnification of 0.49, the NEDT will be increased to 50 mK / $\sqrt{0.49}$ = 72 mK. Before motion blurring occurs, the microbolometer signal can be integrated during 4.4 km / 7 km/s = 0.63 s. After 0.63 s averaging, the NEDT will be reduced to 72 mK / $\sqrt{0.63s * 30Hz}$ = 17 mK for a hypothetical microbolometer without spectral filter. From the ECO spectral filters - illustrated in Figure 19 and quantised by equations 3 - the fractions measured for an ideal black body at 300 K are calculated, and the respective resulting NEDTs are calculated and listed in Table 3.

Table 3. Long-wave Filter fraction and NEDT.

	Band 1	**Band 2**	**Band 3**	**Band 4**	**Band 5**	**Band 6**
Fraction of Black body radiation	0.1087	0.1155	0.1083	0.0908	0.0643	0.0362
NEDT per band (mK)	51.55	50.03	51.66	56.40	67.02	89.3785

3.3. Longwave spectral regression

In [12], the OLR was estimated from a single narrowband irradiance I_{nb} measurement, by the following steps:

1. conversion of the narrowband irradiance I_{nb} to a narrowband brightness temperature T_{nb}
2. conversion of the narrowband brightness temperature T_{nb} to a broadband brightness temperature T_{bb}
3. conversion of the broadband brightness temperature T_{bb} to the OLR

Here we will generalise this approach using 6 narrowband irradiances $I_{nb,i}$, for i=1,...,6. The 6 narrowband irradiances are obtained from the 6 thermal cameras with spectral response illustrated in Figure 19. Using the sigmoid function $s(x)$, with

$$s(x) = \frac{1}{1+e^{-x}} \tag{1}$$

we define the synthetic microbolometer spectral response $f_{mb}(\lambda)$

$$f_{mb}(\lambda) = s((\lambda - 7.5\mu m) * 4) * s(\lambda - 13\mu m) \tag{2}$$

with λ the wavelength, and we define the synthetic narrowband spectral responses $f_{nb,i}(\lambda)$, for i=1,...,6 as

$$\begin{aligned}
f_{nb,1}(\lambda) &= f_{mb}(\lambda) * s((\lambda - 8\mu m) * 10) * s(-(\lambda - 9\mu m) * 10) \\
f_{nb,2}(\lambda) &= f_{mb}(\lambda) * s((\lambda - 9\mu m) * 10) * s(-(\lambda - 10\mu m) * 10) \\
f_{nb,3}(\lambda) &= f_{mb}(\lambda) * s((\lambda - 10\mu m) * 10) * s(-(\lambda - 11\mu m) * 10) \\
f_{nb,4}(\lambda) &= f_{mb}(\lambda) * s((\lambda - 11\mu m) * 10) * s(-(\lambda - 12\mu m) * 10) \\
f_{nb,5}(\lambda) &= f_{mb}(\lambda) * s((\lambda - 12\mu m) * 10) * s(-(\lambda - 13\mu m) * 10) \\
f_{nb,6}(\lambda) &= f_{mb}(\lambda) * s((\lambda - 13\mu m) * 10) * s(-(\lambda - 14\mu m) * 10)
\end{aligned} \tag{3}$$

For a given general spectral irradiance distribution $I(\lambda)$, the narrowband irradiance $I_{nb,i}$ is given by

$$I_{nb,i} = \int I(\lambda) f_{nb,i}(\lambda) d\lambda \tag{4}$$

and the broadband irradiance, also known as the OLR, is given by

$$OLR = \int I(\lambda) d\lambda \tag{5}$$

For the specific case of blackbody radiation, the irradiance distribution is given by the Planck curve and depends only on the temperature T of the blackbody, $I(\lambda) = I_{BB}(T, \lambda)$. We define the brightness temperature $T_{nb,i}$ from an exponential fit to this blackbody radiation:

$$\int I_{BB}(T, \lambda) f_{nb,1}(\lambda) d\lambda \approx (a_i * T_{nb,i})^{b_i} \tag{6}$$

and we define the broadband brightness temperature Tbb from Planck's law:

$$OLR = \sigma * T_{bb}^4 \tag{7}$$

For the general narrowband radiance $I_{nb,i}$ - given by equation 4, the narrowband brightness temperature $T_{nb,i}$ is obtained by inverting the exponential fit from equation 6:

$$T_{nb,i} = \frac{(I_{nb,i})^{\frac{1}{b_i}}}{a_i} \tag{8}$$

and the broadband brightness temperature T_b is obtained by inverting Planck's law:

$$T_{bb} = (\frac{OLR}{\sigma})^{\frac{1}{4}} \tag{9}$$

Similar to [12], we use the libradtran radiative transfer simulation tool, to simulate the narrowband irradiances and OLR for 15 reference scenes, listed in column 1 of Table 4.

Table 4. Longwave reference scenes, OLR, and OLR regression error.

Scene	OLR (W/m^2)	OLR error (%)
US standard - clear sky	257.59	0.21
Tropical - clear sky	284.46	-0.44
Midlatitude summer - clear sky	277.87	-0.25
Midlatitude winter - clear sky	227.95	-0.46
Subarctic summer - clear sky	260.81	-0.11
Subarctic winter - clear sky	197.04	-0.17
US standard - water cloud	214.31	0.61
US standard - thin ice cloud	184.32	0.04
US standard - thick ice cloud	124.75	-0.61
Midlatitude winter - water cloud	200.64	-0.52
Midlatitude winter - thin ice cloud	171.44	-0.49
Midlatitude winter - thick ice cloud	125.25	0.23
Subarctic summer - water cloud	227.57	-0.42
Subarctic summer - thin ice cloud	196.57	-0.07
Subarctic summer - thick ice cloud	142.98	-0.08

For the ensemble of these 15 reference scenes, we regress T_{bb} as a linear function of $T_{nb,i}$:

$$T_{bb} \approx c_0 + \sum_{i=1}^{6} c_i * T_{nb,i} \tag{10}$$

next we evaluate the OLR from T_{bb} using Planck's law - using equation 9. The resulting OLR regression error is given as column 3 of Table 4. It lies within the range +/- 0.61 %.

The general recipee for estimating the OLR from measured narrowband irradiances $I_{nb,i}$, for i=1,...,6 is:

1. convert $I_{nb,i}$ to $T_{nb,i}$ using equation 8
2. estimate T_{bb} from $I_{nb,i}$, using equation 10
3. convert T_{bb} to the OLR, using equation 7

4. Discussion

The monitoring of the Earth Energy imbalance is one of the most critical aspects of mastering our planet's climate change [4,5], and is the main mission objective of the Earth Climate Observatory (ECO) space mission concept. The ECO payload concept consists of four WFOV radiometers as main instruments, targeting an accurate differential measurement of the EEI as the difference of the ISR and the TOR, at a low spatial resolution of approximately 6000 km for a single measurement of the TOR. As auxiliary ECO instruments, cameras are proposed, allowing to spectrally separate the TOR into RSR and OLR, and to resolve the RSR and the OLR at a spatial resolution of at least 5 km at nadir, allowing to distinguish clear-sky from cloudy scenes. In [11] a 1500x1500 RGB CMOS camera was proposed, providing a nadir resolution of approximately 1 km for a single pixel, and allowing to estimate the RSR with a spectral regression error of 3 % at the 2x2 pixel level. In [12] a 750x750 microbolometer camera was proposed, providing a nadir resolution of approximately 2 km, and allowing to estimate the OLR with a spectral regression error of 5 % at the pixel level. In this paper we are introducing some improvements in the ECO camera concept, building further on the [11,12] baseline designs.

For the SW camera, in [11] a single RGB camera - with pixel size of 3.2 μm, and image diameter of 1536 pixels, corresponding to 1536*3.2 μm = 4.9 mm - was used. The accuracy by which the high resolution RSR radiance can be estimated from this camera, is limited to 3 % by the information contained in the three spectral channels, the Red, Green and Blue channels with typical spectral responses shown in Figure 5.

Here we have proposed a dramatic improvement in the number of spectral channels by adopting the IMEC multispectral cameras described in [16], which we adopt as our SW cameras 2 and 3. Camera 2 and 3 provide a total of 31 spectral channels, in the form of a 4x4 VIS and 5x5 VIS-NIR MultiSpectral Filter Array (MSFA) respectively, as illustrated in Figure 6. The IMEC multispectral detectors are based on the CMOSIS CMV2000 detector, with a pixel size of 5.5 μm, and image diameter of 1000 pixels, corresponding to 1000*5.5 μm = 5.5 mm. For the SW camera lense we can use the optical design of [11], with a scaling of 5.5/4.9 = 1.1.

The use MSFA based cameras requires a demosaicing algorithm, for which Deep Learning (DL) based methods are currently an active area of research [23,24]. The quality of the demosaicing will improve if we can provide additional high resolution input information. For this purpose we propose to include SW camera 1, a high resolution RGB camera, based on the CMOSIS CMV12000 detector, with a pixel size of 5.5 μm, and image diameter of 3000 pixels, corresponding to 3000*5.5 μm = 16.5 mm. For this camera, we need a new optical design, which is presented in section 2 and Figure 7.

For the thermal or LongWave (LW) camera, in [12] a single 'broadband' microbolometer camera with spectral response between 8 and 14 μm - see the purple curve in Figure 19 - is proposed. The corresponding OLR spectral regression error is 5 %. Here we propose to use 6 different copies of this basic camera - using the same microbolometer detector array and WFOV LW lense, see Figure 18 - with 6 different filters in front of it. Inspired by the TIRI instrument [19] to be launched as part of the Hera mission [18], we choose 6 adjacent filters with a width of 1 μm, with spectral responses illustrated in Figure 19.

Extending the methodology of [12], with the newly proposed 6 channel LW camera concept, in section 3.3 we evaluate the OLR radiance spectral regression error to be 0.6 %. Thus, comparing our newly proposed LW camera design to the one of [12], by going from 1 to 6 channels, we reduce the OLR spectral regression error from 5 % to 0.6 %.

A detailed analysis of the optical performance of the newly designed high-resolution SW camera, as well as an evaluation of the SNR of all SW cameras and the NEDT of all LW cameras is given in section 2.2. The optical performance is well above what is required for the ECO mission scientific objectives.

5. Conclusions

We propose in this work, an update to the work previously done for the ECO space mission to measure what can be considered as the most essential of all climate variables: the Earth energy imbalance. The proposed payload consists of a combination of highly accurate, but low resolution radiometers measuring the incoming solar radiation and the total outgoing terrestrial radiation in a differential way, enhanced with lightweight uncooled camera systems aiming to separate the total outgoing terrestrial radiation spectrally in reflected solar - or shortwave, and emitted thermal - or longwave radiation, and to increase the spatial resolution to 5 km at nadir or better. Compared to our earlier proposal for the camera system, which consisted of a single SW camera and a single LW camera, we now propose a suite of 3 SW cameras and 6 LW cameras, with strongly improved spectral information content, and with an optical performance that is largely sufficient for the intended application.

Acknowledgments: The work performed by Y.Z was supported by the China Scholarship Council, funding a one year stay of Y.Z at the Royal Observatory of Belgium.

Conflicts of Interest: The authors declare no conflict of interest.

Abbreviations

The following abbreviations are used in this manuscript:

EEI	Earth energy Imbalance
FWHM	Full Width at Half Maximum
OLR	Outgoing Longwave Radiation
RSR	Reflected Solar Radiation
WFOV	Wide Field of View
VIS	Visible
VIS-NIR	Visible and Near-infrared
CMOS	Complementary metal oxide semiconductor
FOV	Field of View
RMS	Root-Mean Square
PSF	Point Spread Function
SNR	Signal to Noise Ratio
LSB	Least significant Bit
NEDT	Noise Equivalent Differential Temperature

References

1. Dewitte, S.; Clerbaux, N. Measurement of the Earth radiation budget at the top of the atmosphere—A review. *Remote Sensing* **2017**, *9(11)*, 1143.
2. Trenberth, K.; Fasullo, J.; Von Schuckmann, K.; Cheng, L. Insights into Earth's energy imbalance from multiple sources. *Journal of Climate* **2016**, *29(20)*, 7495–7505.
3. Von Schuckmann, K.; Cheng, L.; Palmer, M.; Hansen, J.; Tassone, C.; Aich, V.; Adusumilli, S.; Beltrami, H.; Boyer, T.; Cuesta-Valero, F.; Desbruyères, D. Heat stored in the Earth system: where does the energy go? *Earth System Science Data* **2020**, *12(3)*, 2013–2041.
4. Hansen, J.; Nazarenko, L.; Ruedy, R.; Sato, M.; Willis, J.; Del Genio, A.; Koch, D.; Lacis, A.; Lo, K.; Menon, S.; Novakov, T. Earth's energy imbalance: Confirmation and implications. *Science* **2005**, *308(5727)*, 1431–1435.
5. Von Schuckmann, K.; Palmer, M.; Trenberth, K.; Cazenave, A.; Chambers, D.; Champollion, N.; Hansen, J.; Josey, S.; Loeb, N.; Mathieu, P.; Meyssignac, B. An imperative to monitor Earth's energy imbalance. *Nature Climate Change* **2016**, *6(2)*, 138–144.
6. Schifano, L.; Smeesters, L.; Geernaert, T.; Berghmans, F.; Dewitte, S. Design and analysis of a next-generation wide field-of-view earth radiation budget radiometer. *Remote Sensing* **2020**, *12(3)*, 425.
7. Doelling, D.; Keyes, D.; Nordeen, M.; Morstad, D.; Nguyen, C.; Wielicki, B.; Young, D.; Sun, M. Geostationary enhanced temporal interpolation for CERES flux products. *J. Atmos. Oceanic Technol.* **2013**, *30(6)*, 1072–1090. doi:10.1175/JTECH-D-12-00136.1.
8. Loeb, N.; Doelling, D.; Wang, H.; Su, W.; Nguyen, C.; Corbett, J.; Liang, L.; Mitrescu, C.; Rose, F.; Kato, S. Clouds and the earth's radiant energy system (CERES) energy balanced and filled (EBAF) top-of-atmosphere (TOA) edition-4.0 data product. *Journal of Climate* **2018**, *31(2)*, 895–918.
9. S. Kato, N. Loeb, F.R.T.T.D.R.S.H.D.D. Earth radiation budget climate record composed of multiple satellite observations. 2023, pp. IUGG23–4506.
10. Hocking, T.; Mauritsen, T.; Megner, L. Sampling strategies for Earth Energy Imbalance measurements using a satellite radiometer; Earth Energy Imbalance Assessment Workshop, , 2023.
11. Schifano, L.; Smeesters, L.; Berghmans, F.; Dewitte, S. Optical system design of a wide field-of-view camera for the characterization of earth's reflected solar radiation. *Remote Sensing* **2020**, *12(16)*, 2556.

12. Schifano, L.; Smeesters, L.; Berghmans, F.; Dewitte, S. Wide-field-of-view longwave camera for the characterization of the earth's outgoing longwave radiation. *Sensors* **2020**, *21(13)*, 4444.
13. Wu, A.; Xiong, X.; Doelling, D.; Morstad, D.; Angal, A.; Bhatt, R. Characterization of Terra and Aqua MODIS VIS, NIR, and SWIR spectral bands' calibration stability. *IEEE Transactions on Geoscience and Remote Sensing* **2012**, *51(7)*, 4330–4338.
14. Decoster, I.; Clerbaux, N.; Baudrez, E.; Dewitte, S.; Ipe, A.; Nevens, S.; Blazquez, A.; Cornelis, J. Spectral aging model applied to meteosat first generation visible band. *Remote Sensing* **2014**, *6(3)*, 2534–2571.
15. Sterckx, S.; Adriaensen, S.; Dierckx, W.; Bouvet, M. In-orbit radiometric calibration and stability monitoring of the PROBA-V instrument. *Remote Sensing* **2016**, *8(7)*, 546.
16. Geelen, B.; Blanch, C.; Gonzalez, P.; Tack, N.; Lambrechts, A. A tiny VIS-NIR snapshot multispectral camera. *SPIE Advanced Fabrication Technologies for Micro/Nano Optics and Photonics VIII* **2015**, *9374*, 194–201.
17. Weidmann, D.; Antonini, K.; Pino, D.; Brodersen, B.; Patel, G.; Hegglin, M.; Sioris, C.; Bell, W.; Miyazaki, K.; Alminde, L.; Gabriele, A. Cubesats for monitoring atmospheric processes (CubeMAP): a constellation mission to study the middle atmosphere. *SPIE. In Sensors, Systems, and Next-Generation Satellites XXIV* **2020**, *11530*, 141–159.
18. Michel, P.; Küppers, M.; Bagatin, A.; Carry, B.; Charnoz, S.; De Leon, J.; Fitzsimmons, A.; Gordo, P.; Green, S.; Hérique, A.; Juzi, M. The ESA Hera mission: detailed characterization of the DART impact outcome and of the binary asteroid (65803) Didymos. *The Planetary Science Journal* **2022**, *3(7)*, 160.
19. Okada, T.; Tanaka, S.; Sakatani, N.; Shimaki, Y.; Arai, T.; Senshu, H.; Demura, H.; Sekiguchi, T.; Kouyama, T.; Kanamaru, M.; Ishizaki, T. Calibration of the Thermal Infrared Imager TIRI onboard Hera. In European Planetary Science Congress, 2022, pp. EPSC2022–1191.
20. Schmetz, J.; Pili, P.; Tjemkes, S.; Just, D.; Kerkmann, J.; Rota, S.; Ratier, A. An introduction to Meteosat second generation (MSG). *Bulletin of the American Meteorological Society* **2002**, *83(7)*, 977–992.
21. Ouaknine, J., V.T.N.B.F.U.F.S.H.P.D.Y.I.S.P.P.R.J.; Riguet, F. The FCI on board MTG: optical design and performances. 2017, Vol. SPIE Vol. 10563, pp. 617–625.
22. Tissot, J.; Tinnes, S.; Durand, A.; Minassian, C.; Robert, P.; Vilain, M. High-performance uncooled amorphous silicon VGA and XGA IRFPA with 17µm pixel-pitch. *SPIE. In Electro-optical and infrared systems: Technology and applications VII* **2010**, *7834*, 147–154.
23. Arad, B., T.R.Y.R.M.N.B.A.W.Y.W.X.F.Z.X.C.Z.F.; Liu, S. NTIRE 2022 spectral demosaicing challenge and data set. 2022, pp. 882–896.
24. Zeng, H.; Feng, K.; Huang, S.; Cao, J.; Chen, Y.; Zhang, H.; Luong, H.; Philips, W. MSFA-Frequency-Aware Transformer for Hyperspectral Images Demosaicing, 2023, [arXiv:eess.IV/2303.13404].